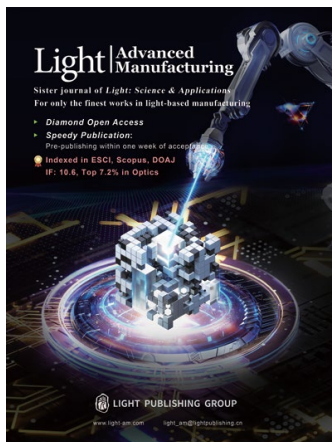


Accepted Article Preview: Published ahead of advance online publication



## Rapid fabrication of optical elements for sensing applications using a standard SLA printer

María Amparo Hernández-García, Knut Rurack, Jérémy Bell

Cite this article as: María Amparo Hernández-García, Knut Rurack, Jérémy Bell. Rapid fabrication of optical elements for sensing applications using a standard SLA printer. *Light: Advanced Manufacturing* accepted article preview 12 January, 2026; doi: 10.37188/lam.2026.024

This is a PDF file of an unedited peer-reviewed manuscript that has been accepted for publication. LAM are providing this early version of the manuscript as a service to our customers. The manuscript will undergo copyediting, typesetting and a proof review before it is published in its final form. Please note that during the production process errors may be discovered which could affect the content, and all legal disclaimers apply.

Received 22 September 2025; revised 9 January 2026; accepted 12 January 2026;  
Accepted article preview online 12 January 2026

## Rapid fabrication of optical elements for sensing applications using a standard SLA printer

### Authors

María Amparo Hernández-García, Knut Rurack, Jérémy Bell

*Bundesanstalt für Materialforschung und -prüfung, Richard-Willstätter-Str. 11, 12489 Berlin, Germany*

*jeremy.bell@bam.de*

ORCID:

J. Bell: <https://orcid.org/0000-0003-1861-1670>

K. Rurack: <https://orcid.org/0000-0002-5589-5548>

M.A. Hernández-García: <https://orcid.org/0009-0003-0806-4498>

### Abstract

The demand for compact, high-performance optical components has driven the development of increasingly sophisticated and miniaturized optical elements, often requiring complex and costly fabrication methods. In this study, we propose a cost-effective and accessible methodology for the fabrication of lenses and free-form optics using a commercially available stereolithography (SLA) 3D printer. A systematic characterisation of six transparent photopolymer resins was conducted in terms of their spectroscopic, optical, and morphological properties, i.e., surface and dimensional properties. The evaluation encompassed parameters such as transmittance, autofluorescence, refractive index, and surface roughness. A straightforward yet resilient printing and post-treatment protocol was formulated, facilitating the fabrication of optical components with over 80% transmittance, minimal intrinsic fluorescence, and surface quality that is compatible with exacting optical applications. The fabricated components demonstrated excellent dimensional fidelity to digital designs and high reproducibility. To demonstrate the versatility of this approach, aspherical, miniaturized, and free-form lenses were designed and integrated into three fluorogenic sensing systems, including oil (strip based) and chlorine (microfluidic based) detection platforms, as well as a smartphone-based SARS-CoV-2 biosensor. The integration of customized 3D-printed optics has been demonstrated to enhance signal collection and readout performance, thereby highlighting the potential of this approach to democratize the rapid prototyping and deployment of miniaturized optical systems. This work represents a significant advancement in the field of additive manufacturing, particularly in relation to the development of functional photonic devices. Furthermore, it opens new prospects for sensor applications in biosensing, microfluidics, imaging, and integrated optics.

### Keywords

3D-printing, Free-form, Prototyping, Fluorescence, Sensor, Optical resin, Surface-finishing

## Introduction

Recent advances in optical sensing, imaging, and photonic devices have led to growing demand for optical components that combine compactness, versatility, and high performance.<sup>1, 2</sup> Free-form optics—optical elements with asymmetrical, non-rotationally invariant surfaces—have established themselves as a key technology in this field, as they offer unparalleled flexibility in adapting light propagation, minimizing system size, and enhancing device functionality.<sup>3</sup> Compared to conventional spherical or aspherical elements, free-form optics offer greater freedom in tailoring the surface geometry across multiple axes, allowing designers to correct complex, field-dependent aberrations and significantly reduce the number of elements in a system. In contrast to conventional lenses, where the surrounding device often has to be adapted to predetermined geometries, free-form optics offer a more flexible approach. They can be shaped to meet the mechanical, electrical, or ergonomic requirements of a specific application, allowing for significantly greater design freedom, especially in scenarios where non-optical components are difficult to modify. Consequently, free-form optics enable novel compact architectures for applications ranging from biomedical imaging to autonomous sensing and augmented reality where performance must be maintained within strict size, weight, and power constraints.<sup>4</sup>

However, the fabrication of free-form optical elements remains a major challenge. Standard techniques such as ultraprecision machining, polishing, and ion beam processing are limited by material compatibility, surface complexity, and production costs, restricting their use to specialized laboratories and high-end industries.<sup>5</sup> Similarly, laser-based fabrication methods, while offering high precision, involve high acquisition costs, stringent environmental requirements, and considerable technical expertise, also limiting their use to specialized facilities. Furthermore, the need for iterative prototyping during the optical design process increases time and cost, thereby hindering innovation. Recently inkjet printing methods demonstrated their capacity to manufacture optical component,<sup>6, 7</sup> but devices and resins remain expensive and dedicated to specialists. To overcome these limitations, additive manufacturing, particularly liquid resin vat photopolymerization techniques such as stereolithography (SLA) and digital light processing (DLP), has increasingly attracted attention as a promising platform for the fabrication of complex optics.<sup>8-10</sup> These methods enable the rapid, cost-effective, layer-by-layer fabrication of transparent polymeric structures with virtually any geometry, using benchtop printing systems that are widely available and affordable even for non-specialists. The first printers appeared in the 1980s, but the technology's popularity did only grow massively after the expiration of the first patent.<sup>11</sup> This combination of simplicity, low cost, and design flexibility provides a powerful tool for iterative, on-demand prototyping and small-scale production.<sup>12</sup>

Despite these promising prospects, several critical challenges remain before 3D-printed optics can meet the stringent requirements of optical applications. The quality of printed elements is often compromised by several factors, including insufficient optical clarity, high surface roughness, and material autofluorescence. All these issues can contribute to a reduction in device performance. Furthermore, the refractive index of photopolymer resins plays a critical role in determining the light-guiding, refracting, or focusing properties of printed optical components. However, there is a lack of available data on commercial materials in this field.<sup>13-15</sup>

Due to our long-standing focus on the development of miniaturized analytical assays and devices for onsite (bio)chemical analysis and sensing—primarily utilising fluorescence detection—we require cost-effective, application-specific optical systems for the readout of test strips, lateral flow assays or microfluidic chips. These systems require light-tight housings and integrated excitation and emission

optics, which we often manufacture using 3D printing. In particular, the fabrication of free-form, transparent optical elements with minimal autofluorescence (when excited in the deep blue) has become a key aspect of our work. To ensure affordability and accessibility, we focus on the use of commercially available resins and filaments that are compatible with desktop 3D printers. This motivated us to conduct a comprehensive spectroscopic, optical, and morphological study of six transparent resins suitable for LCD-based SLA printing, which are readily available from online retailer platforms. We characterized their light transmittance, autofluorescence, refractive index and surface quality, and established a robust post-processing protocol that significantly improves optical performance.

Based on these findings, a simple and fast method for producing optical elements was developed and validated through practical applications. Three fluorescence sensor systems from previous works—each requiring miniaturized, aspherical or free-form lenses—were selected as test cases.<sup>16-18</sup> In these systems, the original glass optics were either replaced by 3D-printed resin replicas (“twins”) or by newly designed free-form optics tailored to the specific sensor geometry. The resin twin lenses showed a high match with their glass counterparts, while the custom-designed free-form optics led to a significant improvement in performance. As an introductory proof of concept, Figure 1 shows the rapid prototyping of a retroreflector prism, highlighting the potential of this approach to make the development of low-cost, customized optical components widely accessible. This work impressively demonstrates how 3D printing workflows that can be deployed in almost any laboratory can support the advancement of integrated optics, biosensing, microfluidics and other light-based technologies.

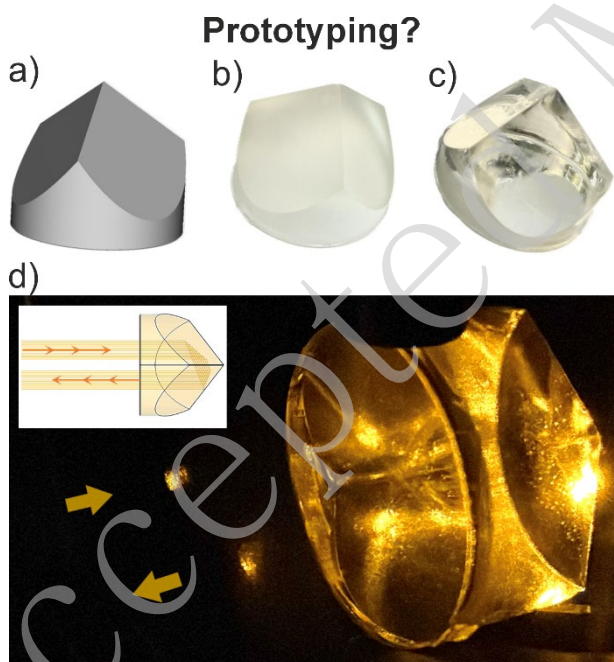


**Figure 1.** Successive stages in the fabrication of a retroreflector prism for optical applications: a) computer-aided design; b) SLA printed element; c) element after post-treatment; d) retroreflection of a laser beam at 589 nm by the manufactured optical element shown in c).

## Experimental section

### *Resins and devices*

Six colourless commercial resins were purchased: *Siraya tech simple – Water washable (resin 1)* (Siraya tech); *Superfast clear (resin 2)* (3D Materials); *High clear resin (resin 3)* (Anycubic); *Clear impact (resin 4)* (Liqcreate); *High Clear Resin (#3124) (resin 5)* (IFUN); *Standard photopolymer resin translucent (resin 6)* (Elegoo).

The characterization of the candidate materials was performed with printed bulk rectangular cuboid blocks in the shape of a conventional 10 mm-cuvette external dimensions (12.4 × 12.4 × 55.0 mm). Each element was printed on a Phrozen Sonic mini 8K printer (Phrozen) in normal atmosphere. The printed parts are constantly immersed in the liquid resin during the printing process, but are not exposed to directly to air during this process. The printing was followed by a washing step (2 min) with isopropanol (isopropyl alcohol, IPA; Labsolute) to eliminate the excess of resin from the surface of the blocks. For post-processing, to eliminate the printing-related surface artefacts as effectively as possible, the raw objects were coated with mother resin, which was applied using a pneumatic atomisation technique with an airbrush pistol (AFC-101A Double action airbrush pistol Nozzle, diameter 0.35 mm, Conrad) connected to compressed air. At working pressures of 1–3 bar, the 0.35 mm nozzle cap produces a conical spray of droplets of 30–60 µm, consuming approximately 1 mL s<sup>-1</sup> of resin. With a working distance of approximately 10 cm, the spray coated area is around 3 cm in diameter. The smaller objects were coated using a silicon brush to obtain a more efficient finish. In a second step, the coating of the thinly applied resin was cured through photo-polymerization by UV light irradiation in a curing machine (Wash and cure machine 2.0, 405 nm wavelength, Anycubic). For finishing, another washing step (2 min) with IPA was applied, removing possible traces of excess resin, dried with compressed air and followed by a second UV light curing. All the photo-polymerization steps carried out during the post-treatment were performed under normal or inert atmosphere, see details in the *Results and discussion* section.

The printing parameters were selected according to the specifications of the respective manufacturer and refined iteratively to obtain the best possible printing result for the raw element. An opensource 3D design software (FreeCAD) was used for designing the elements and exporting the data to the slicer software (Chitubox, CBD-Tech) for the setting of the printing parameters. The photo-polymerization during the printing process took place under sequential LCD irradiation at 405 nm of the design slices. In the same way, the photo-polymerization during the post-treatment was carried out under constant irradiation at 405 nm.

### *Resin characterization*

The optical transmittance of the resins was recorded with a Specord 210 spectrophotometer (Analytik Jena). To study the materials' autofluorescence, an excitation-emission matrix (EEM) analysis was carried out with a Fluoromax 4 fluorometer (Horiba). The excitation range was 400–600 nm (10 nm step size) and the emission was scanned in the range of 410–850 nm (1 nm step size). To avoid inner filter effects (light absorption, scattering, reflection or shielding) that might appear when the fluorescence of bulk blocks with a potentially too high optical density is measured in the conventional 90° configuration, the blocks were measured in front-face configuration with perpendicular excitation to the block surface and an emission collection with angle of 30° respective to the irradiated surface, collecting only the emission from the surface of the excited sample.<sup>19, 20</sup>

The refractive index was obtained with a customized setup consisting of a 5 mW 589 nm- or 498 nm-laser module as light source and a 3D printed holder with positioning clamps for reproducible mounting and positioning of the optical element. Especially the 589 nm-laser module was used as it corresponds best to the sodium D line which is the standard wavelength used for the determination of the refractive

index of glasses.<sup>21</sup> The refractive index of the resin,  $n_2$ , was calculated manually according to Snell's law

$$n_1 \sin \theta_1 = n_2 \sin \theta_2$$

where  $n_1 = 1$  is the refractive index of air,  $\theta_1 = 45^\circ$  is the angle of the incident laser beam and  $\theta_2$  is the angle of the refracted beam in the printed optical element.  $\theta_1$  and  $\theta_2$  were obtained from photographs of the beam path taken with a camera mounted perpendicularly to the beam and traced with the aid of a drawing software (CorelDraw, Corel).

Surface roughness was studied with a laser scanning microscope (Lext OLS5000, Olympus) using x50 magnification and the respective parameters were calculated using 4 random working areas of  $258 \times 258 \mu\text{m}^2$ .

To assess the dimensional accuracy (match of 3D-designed and printed objects) and the dimensional reproducibility of the 3D printed structures, parallelism and thickness of the elements were measured with a digital indicator (Digi-met, Helios Preisser) and a digital ruler (digiMax, Wiha), respectively. The dimensional gauges were performed between the parallel sides of the blocks.

#### *Miniaturized analytical devices*

Two miniaturized opto-analytical devices previously published by us were replicated with the equivalent 3D printed optical components following the developed protocol and **resin 1**. The first one was a fluorometric test strip-based assay for hydrocarbon detection (Figure S15).<sup>16</sup> Fluorescence was generated using a standard 430 nm light-emitting diode (LED, LED 430-06, Roithner Lasertechnik), which was filtered through a bandpass filter (65622, Edmund Optics) mounted at an angle of  $130^\circ$  to the surface of the strip. The emission from the test strip was collected perpendicularly to the strip, passed through a long-pass filter at 455 nm (5CGA-455, Newport) and focused by an aspheric condenser lens (ACL25416U, Thorlabs) into an optical fibre bundle (BFL200HS02, Thorlabs) connected to a USB spectrometer (USB2000+, ILX-511B detector, OceanOptics). The signal was acquired in the range of 460–650 nm and processed on a laptop computer with the SpectraSuite software (OceanOptics). The second system was a microfluidic chip-based device for monitoring chlorine levels in pools (Figure S16).<sup>17</sup> The excitation source was a 490 nm LED (LED 490-06, Roithner Lasertechnik) filtered with a 500 nm short-pass filter (FESH0500, Thorlabs) and focused on the microfluidic chip with a plano-convex lens (LA1540, Thorlabs). The fluorescence from the chlorine-reactive fluorescent probe flowing through the chip was collected into an optical fibre bundle (BFL200HS02, Thorlabs) after passing through a 515 nm long-pass filter (OG515, Edmund Optics) and focusing with a plano-convex lens (LA1540, Thorlabs). The fluorescence was analysed with the USB spectrometer as above and signal acquisition in the range of 510–650 nm was also made in a similar manner.

For both setups, calibration curves were obtained for increasing concentrations of diluted lubricant oil (LiquiMoly) or sodium hypochlorite (Labsolute) in water, respectively, first with the commercial lenses and then with the replicas prepared from **resin 1**. Three repeat measurements were made in every case.

For the third miniaturized device, three newly designed free-form optics were added to improve the optical readout of a smartphone-based assay for the rapid detection of microbial contamination of fuels (Figure S17).<sup>18</sup> The new lenses were manufactured following the developed protocol and using **resin 1**, before being mounted inside a 3D-case, which was printed with black PLA filament using an Ultimaker 3 printer (Freeform4U). For excitation, a 465 nm LED (RLS-B465, Roithner LaserTechnik) was driven by a DC current of 20 mA drawn from the smartphone's battery via a USB on-the-go (OTG) connection. A  $469 \pm 18$  nm bandpass filter (FF01-469/35-25, Semrock) was placed in the excitation

beam and a 500 nm long-pass filter (FEL0500, Thorlabs) between strip and the smartphone's CMOS back camera, which was used to collect the emission. Photographs were taken with a Samsung Galaxy S7. The smartphone camera was set with a shutter speed of 1/10 s, an ISO gain at 1600 and a white balance at 5000 K. The focus was manually controlled; macro focus without lenses, infinite focus with the lenses. The molecular beacon and complementary RNA sequence were purchased from Eurofins.

## Results and discussion

### *Optimisation of the 3D printing process*

SLA printing builds 3D objects by curing thin layers of resin using structured light exposure,<sup>22, 23</sup> making it a promising technique for manufacturing transparent optical components with complex geometries.<sup>24</sup> However, commercially available resins and standard printer settings are typically optimized for structural applications rather than optical quality, so printed objects often lack the transparency required for optical elements. To assess the suitability of commercially available transparent resins, six commercial products were selected (see Experimental Section) and printed using the manufacturer's standard settings. The resulting rectangular cuboid blocks often showed internal air bubbles and a cloudy, uneven appearance. To improve printing quality, certain process parameters were systematically modified (Table S1). In particular, reducing the speed for all layers significantly improved layer adhesion and minimised the trapping of bubbles (Figure S1); but to preserve clearness and avoid yellowing of the resin, rapid printing was necessary.

However, even with customized settings, the printed blocks initially had a cloudy, translucent appearance (Figure S2), which did not correspond to the designation of the resins yielding "clear" or "transparent" prints. Microscopy analysis revealed that the cause was the stair-stepping effect, a well-known artefact of layer-by-layer manufacturing that results in surface roughness that scatters light (Figure 2a). These results stressed the importance of adjusting both the printing process and the subsequent post-treatment steps to meet optical quality requirements (Figure S3).

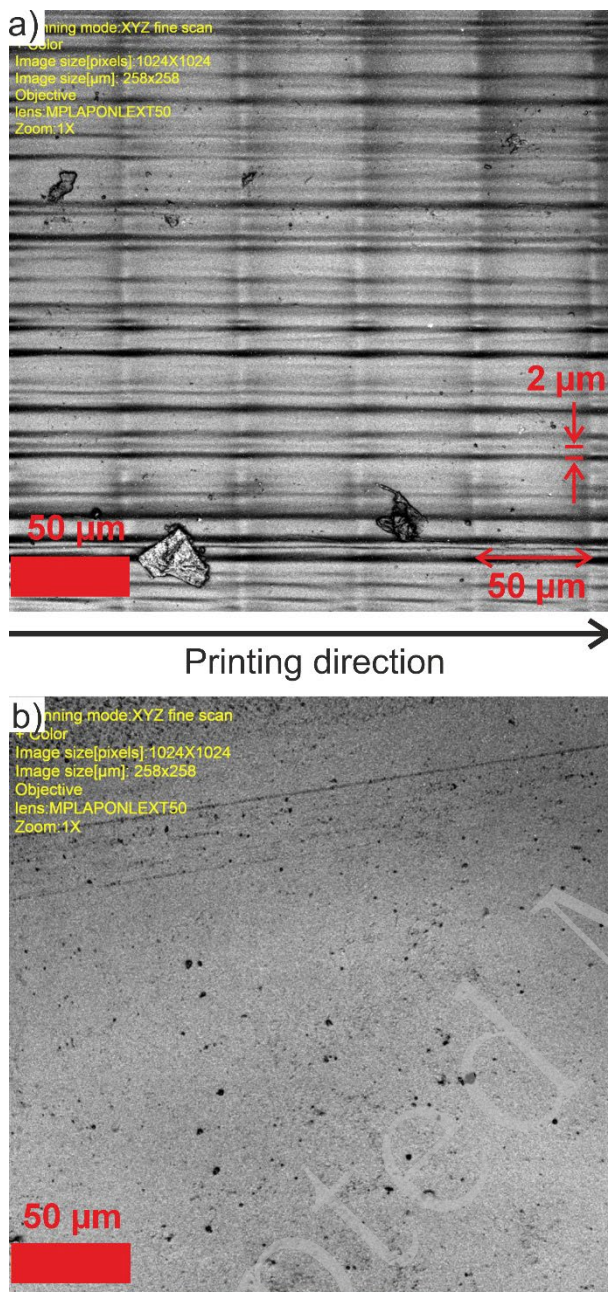


**Figure 2.** Laser scanning microscope image ( $258 \times 258 \mu\text{m}$ ), with nominal magnification of  $\times 50$ , of a 3D printed rectangular cuboid block a) without post-treatment and b) after post-treatment. The black arrow shows the printing direction in which layers  $50 \mu\text{m}$  width are built perpendicularly to the printing direction.

As Figure 2a reveals, the wider recurrent structural patterns on the surface of the object correspond to the pre-set printing layer thickness (approx.  $50 \mu\text{m}$ , in printing direction), while the narrower features of approx.  $2 \mu\text{m}$  are presumably connected to the foci of the microlens array of the light source. Hence, to increase the transparency and smooth the surface a post-treatment is necessary.<sup>25</sup>

Most reported post treatment procedures are abrasive techniques, which are ultimately followed by coating with a varnish.<sup>26, 27</sup> However, without precision instruments for abrasion, the reproducibility of such methods is hard to control. In addition, the varnish coating results in a thin layer of material on the printed substrate that possesses different optical properties, which is undesirable as it can

introduce further complexity, for instance, in case of unmatched refractive indexes. Thus, an alternative post-treatment procedure was developed, utilizing the same UV curable polymerization mixture and applying it in a micrometric layer.<sup>28</sup> For this purpose, the surface of the printed objects was coated with the respective resin using a pneumatic atomisation technique, whereby fine droplets produce a very homogeneous layer that largely levels out the ridges and valleys caused by printing, resulting in much smoother surfaces. Smaller printed objects were coated using a silicon brush to remove excess of resin applied during spray coating and obtain better finish. This method allow to coat indefinite geometries without the limitation that other coating techniques offer, for example, spin-coating, in which a planar surface is needed to apply the resins.<sup>14</sup> A single coating step resulted in a significant improvement of the surface smoothness and the optical properties of the object with respect to the raw object as shown by the laser scanning microscopy images in Figure 2b and Figures S5-9, the macroscopic net effect being visible in Figure S2. To quantify the post-synthetic improvement, four commonly employed roughness parameters were considered and determined: the root mean square deviation (Rq) and arithmetic mean deviation (Ra) within the sampling length (258  $\mu\text{m}$ ) as well as the root mean square height (Sq) and arithmetic mean height (Sa) within the evaluation area (258  $\times$  258  $\mu\text{m}$ ).<sup>29</sup> Table 1 shows the average of the roughness parameters of five bulk elements printed from the commercial resins. The post-treatment applied during the manufacturing process achieves low and comparable surface roughness values, similar to those obtained through more complex polishing techniques such as laser ablation, with a surface roughness range of 0.12–0.61  $\mu\text{m}$ , using different types of polymers.<sup>30</sup> Manufacturing processes for optical glass, such as N-BK7, can achieve higher grades of surface qualities and lower surface roughness values, yet it involves more complex and sophisticated instrumentation.<sup>31, 32</sup> This translates into higher costs, the need for qualified personnel, and longer manufacturing times.<sup>33</sup>

**Table 1.** Roughness average of six 3D printed elements manufactured from six different optically suitable commercial resins for LCD 3D printing using a laser scanning microscope.

Resins	Ra (nm)	Rq (nm)	Sa (nm)	Sq (nm)
resin 1	33 $\pm$ 96	52 $\pm$ 148	34 $\pm$ 13	126 $\pm$ 92
resin 2	14 $\pm$ 19	20 $\pm$ 29	17 $\pm$ 3	50 $\pm$ 16
resin 3	15 $\pm$ 20	22 $\pm$ 35	16 $\pm$ 3	54 $\pm$ 13
resin 4	16 $\pm$ 21	23 $\pm$ 34	20 $\pm$ 7	68 $\pm$ 44
resin 5	21 $\pm$ 28	33 $\pm$ 55	24 $\pm$ 3	84 $\pm$ 18
resin 6	15 $\pm$ 15	20 $\pm$ 28	25 $\pm$ 25	44 $\pm$ 39

Structurally, the manufactured optical elements exhibited dimensional deviations in the micrometre range and parallelism deviations on the order of a few arcminutes (Table S2). This latter deviation is due to a thin meniscus of excess coating resin that accumulates at the lower edge and causes a slight tilt, contributing to angular deviation. In the centre of the optical element, the measured parallelism was  $4.3 \pm 1.6$  arcminutes, which is within the typical specification range for commercial optics (often  $\leq 1\text{--}5$  arcminutes).<sup>34, 35</sup> This precision meets industry-level tolerances. For example, precision glass moulding processes routinely achieve wedge tolerances of around 1 arcminute and position alignment errors of a few arcminutes<sup>36</sup>. Similarly, the deviation between the printed object and its digital design was 22  $\mu\text{m}$  for a set of five cuboids, which corresponds to the expected profile errors in commercially available polymer optics, where dimensional tolerances are often within  $\pm 10\text{--}50$   $\mu\text{m}$  depending on the

size of an object and the process parameters.<sup>34,35</sup> In addition to the cuboids, a set of 10 replicas of a standard plano-convex lens was manufactured following the same protocol (Figure S4). The obtained optical resin elements showed similar deviation to the commercial glass lens from the design dimension. The respective deviations in height were 154 and 110  $\mu\text{m}$  for resin 1 and commercial glass, respectively, and 147 and 40  $\mu\text{m}$  for the diameter (Table S2). This slightly bigger deviation in diameter is presumably due to a slight excess of resin accumulating at the bottom edge of the lens. In contrary, the coating of resin on the spherical part of the lens appeared optimal and the obtained radius of curvature was  $13.07 \pm 0.05$  mm for a design with a radius of 13.1 mm.

Besides the surface and structural parameters, the inner properties of the printed elements were also checked for compatibility with optical applications. First, the optical transparency was analysed (Figure 3). Indeed, optical elements require maximal transmittance in the selected spectral range, avoiding power losses. The light transmittance of six rectangular cuboid blocks printed with the commercial resins was evaluated, as it is a discriminatory factor for their use in the optical devices of our test cases. The elements printed with **resins 1–5** showed transmittances of 85% for wavelengths above 450 nm, but the transmittance of **resin 6** was less than 80% below 500 nm. For the first five resins, the values are only slightly lower than those for standard optical materials such as poly(methyl methacrylate) (PMMA) or N-BK7 glass, which commonly possess transmittances of approx. 90% for 10 mm optical depth.<sup>37,38</sup>

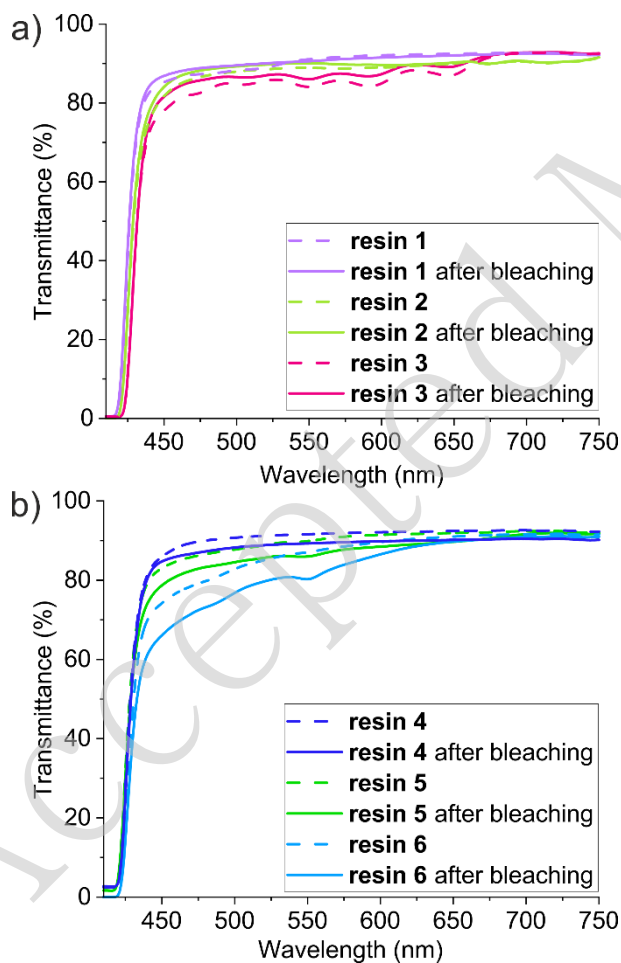


**Figure 3.** Transmittance spectra of 12.4 mm thick rectangular cuboid blocks before (dashed line) and after dual wavelength irradiation (line) at 450/550 nm, fabricated from six different commercial resins and post-treated in inert atmosphere: a) **resin 1** (light purple), **resin 2** (light green), and **resin 3** (pink); b) **resin 4** (dark blue), **resin 5** (dark green), and **resin 6** (light blue).

The limited transmittance can be due to the disruption of the polymerization process by oxygen inhibition, where interaction of the photo-initiators with the oxygen present in air can induce the formation of inactive peroxy radicals, such as hydroperoxides, or by scavenging the formed radicals.<sup>39-42</sup> For example, the photo-initiator 2,2-dimethoxy-2-phenylacetophenone frequently leads to photo-yellowing because of cleavage and formation of coloured recombination products during prolonged UV irradiation.<sup>43, 44</sup>

To prevent further detrimental processes from occurring after post-treatment in air, the printed and coated objects were irradiated for 24 h at 450 nm and 550 nm with 36 W, causing the excess of photo-initiator and oxidized reaction products to photo-bleach.<sup>45-47</sup> As shown in Figure 3, the bleaching led to an increase of the light transmission of **resins 1–3** in the range 440–580 nm. However, **resins 4–6** exhibited an attenuation of optical transmittance in the range 440–700 nm, which was most dramatic in the case of **resin 6**.

After identifying the potentially problematic effects of atmospheric oxygen on the properties of the finished objects, we investigated the extent to which post-treatment of the printed objects in an inert atmosphere (N<sub>2</sub> or Argon) could be beneficial (Figure 4, Figure S10). The first finding was that no noticeable difference was observed between argon or nitrogen with high transmittance from 420 to above 1100 nm for **resin 1**. While the elements post-treated under air atmosphere needed 20–30 min of curing time and exhibited a fragile surface, those cured under inert atmosphere only needed 1 min curing, resulting in a more rigid surface. Some resins even exhibited shrinkage of the surface coating after less than a minute of curing (Figure S11). This phenomenon could be due to the shrinkage the polymeric matrix tends to undergo when there is a reduction of the intermolecular distance upon conversion of the free monomer molecules (Van der Waals forces distances) to covalent bond during polymerization and crosslinking.<sup>48,49</sup> Therefore, the curing time and conditions need to be adapted for every single resin. Attempts to cure in the dark without UV light, but by heating in an oven, resulted in yellowish and brittle elements and were therefore not continued (Figure S12) In addition, the undesirable formation of yellowish products decreased drastically upon curing in inert atmosphere. The transmittance of all the resins increased significantly apart for **resin 6**. The resulting transmittance for **resins 1–5** reached up to 90%, much closer to standard optical materials properties.

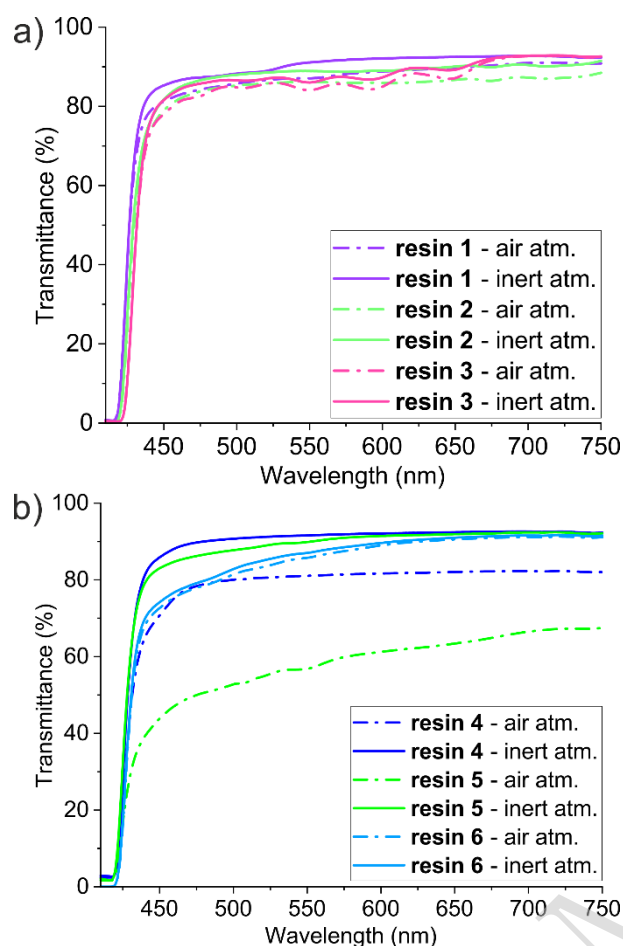


**Figure 4.** Transmittance spectra of six rectangular cuboid blocks of 12.4 mm thickness fabricated from six commercial resins post-treated in air (dashed line) and inert atmosphere (line): a) **resin 1** (light purple), **resin 2** (light green), and **resin 3** (pink); b) **resin 4** (dark blue), **resin 5** (dark green), and **resin 6** (light blue).

For optical elements in general, and especially for optics used in low light application such as fluorescence, the material must have virtually no intrinsic fluorescence background, i.e., autofluorescence should be minimal. The presence of photo-initiators or photo-stabilizers able to emit fluorescence can potentially lead to such undesirable background. Therefore, we recorded excitation-emission matrices (EEM) of **resins 1–5** (Figure 5, Figure S13). Low fluorescence signals were measured for **resins 1–3**, especially for **resin 2**, for which there is virtually no fluorescence in the entire spectral working range. **Resin 1** exhibited a fairly intense fluorescence localized at 430–520 nm upon excitation at 420 nm, while **resin 3** showed a weak fluorescence between 440–540 nm for excitation wavelengths between 410–440 nm. **Resins 4–5** exhibited the highest fluorescence intensity, in the 430–550 nm range upon excitation between 410–440 nm. Although the exact chemical composition of the resins is not known, the sources for the fluorescence are most likely the photo-initiator, since most of them have a sizable molar absorption coefficient in the blue range, corresponding to the LCD printer's irradiation wavelength, in our case 405 nm,<sup>50-52</sup> or the photo-stabilizers, also absorbing in the UV.

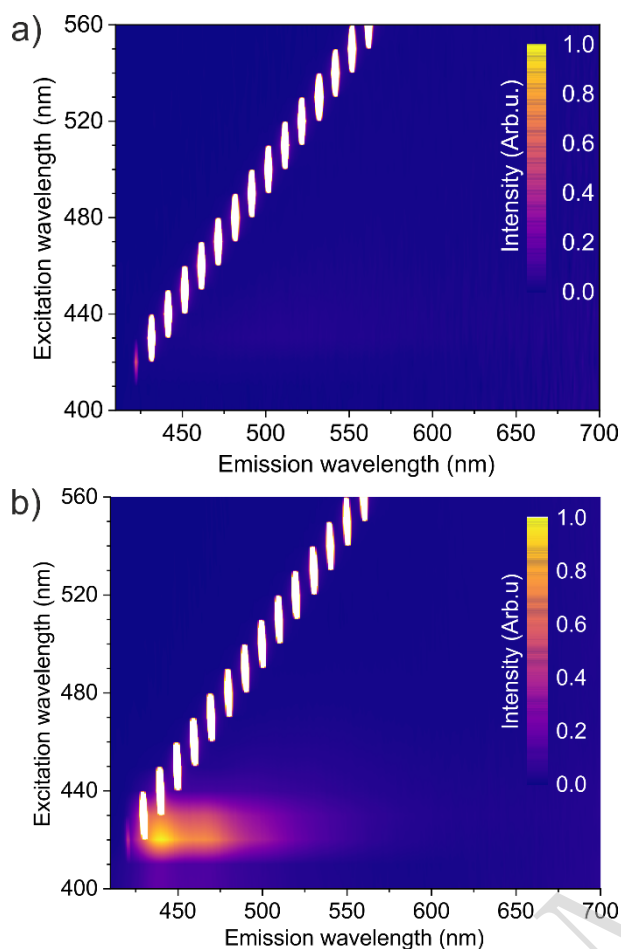


**Figure 5.** Front-face excitation-emission-matrices of rectangular cuboid blocks from a) **resin 2** and b) **resin 4**. Matrices built by successively recording emission spectra within the 410–700 nm range at increasing excitation wavelengths between 400 and 560 nm with steps of 10 nm.

In addition, upon storage in the dark at room temperature in air for two years, the manufactured cuboids showed good environmental stability over time, with an only slight decrease in both, transmittance and autofluorescence (Figure S14).

The last materials property that is important for optical elements is the refractive index (RI). The RI will determine how the light is refracted by the element and consequently determine the optical component design and the light output direction. The calculated RI for **resins 1–5** ranged from 1.44 to 1.53 at 589 nm and 1.50 to 1.52 at 498 nm (Table S3). These values are similar to standard optical polymers (e.g., PMMA or polycarbonate) and optical glasses (e.g., N-BK7) which possess RIs of approx. 1.5.<sup>53</sup> This is an advantageous feature because existing design for such materials could be directly transferred to the manufacturing with the newly developed method, affording virtually identical optical behaviour.

#### *Rapid assay test cases*

To demonstrate that the optical components manufactured using the post-processing method developed here can compete with conventional optics in terms of performance, we replicated two miniaturised analytical devices we had previously published with the respective 3D-printed optical

elements. In addition, we designed a new optical system to improve the sensitivity of a third assay and printed the necessary elements, confirming the improved performance in the experiment.

The first test case was a rapid assay for the detection of total petroleum hydrocarbons (TPHs) in water and soil.<sup>16</sup> In brief, the assay uses a fluorometric test strip that is sterically coated with a fluorescent molecular rotor dye which exhibits high fluorescence intensity when TPHs are present. For water samples, the protocol involves adding 160  $\mu$ L of cyclohexane as auxiliary solvent to 40 mL of the water sample, shaking the mixture (1 min) and placing a test strip on its surface to collect the oil. The fluorescence of the strip is then recorded immediately with the device as described in the Experimental Section, and the integrated intensity is compared to a reference strip to calculate the ratio. The optical setup included a commercial aspheric condenser lens which could be easily manufactured following the method described above with **resin 1** (Figure S15, Movie S1). Two calibration curves using the previously described test strips were acquired, one with the commercial lens and the other with the 3D printed twin. As shown in Figure 6a, the two calibration curves measuring the fluorescence response of the strip upon increasing concentrations of TPHs showed identical trends and a comparable standard deviation (total relative error method).<sup>54</sup>

Likewise, a microfluidic device for the determination of water chlorination levels was built with two small lenses (0.5 inches diameter) with focal length of 15 mm for in-flow probe excitation and emission collection (Figure S16, Movie S2).<sup>17</sup> Both small twin lenses of the commercial ones were manufactured. This assay integrates a microfluidic system, a fluorescent indicator dye which reacts specifically with free and other reactive chlorine species. The device's design allows for precise mixing of reagents and sample, followed by fluorescence detection, enabling real-time monitoring of water chlorination levels with the fluorescence signal increasing proportionally to the concentration of chlorine species. As shown in Figure 6b, matching responses were obtained for both setups, with slightly higher repetition errors for the glass lenses that could be due to their enhanced capacity to collect environmental light.

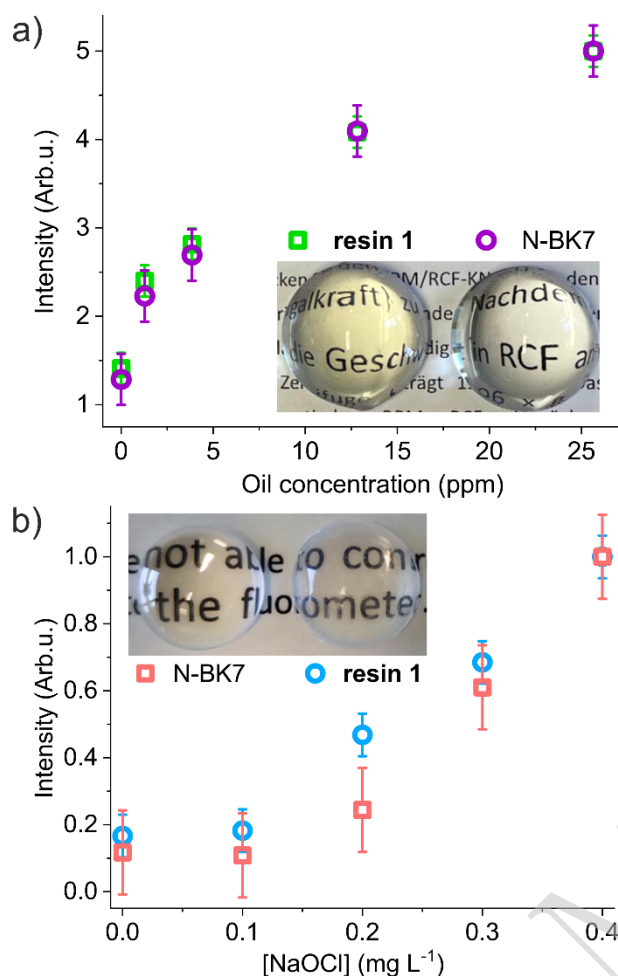


**Figure 6.** Response of two miniaturized analytical devices built with glass lenses (purple and red) and **resin 1** lenses (green and blue): a) test-strip based opto-sensor for hydrocarbon detection with a photograph of the aspheric condenser lenses ( $\varnothing = 25.4$  mm) manufactured with **resin 1**, following the method developed here, and made from NBK-7, obtained from the manufacturer (ACL25416U, Thorlabs); b) microfluidic sensor for chlorination levels in water with a photograph of the two small convex lenses ( $\varnothing = 12.7$  mm) manufactured with **resin 1**, following the method developed here, and made from NBK-7, obtained from the manufacturer (LA1540, Thorlabs).

The third test case concerns an improvement of the device initially developed for a dip-stick assay for the rapid, on-site detection of microbiological fuel contamination.<sup>18</sup> The assay utilizes dip sticks that embed core/shell particles in which the shell is functionalized with molecular beacons. The assay works by detecting the presence of genomic DNA from bacteria and fungi commonly found in contaminated fuels. When this DNA is present, the strands interact with the molecular beacons, leading to a change in fluorescence that can be quantitatively assessed with the optical detection device, indicating the presence of microbial contamination. This system provides a portable and straightforward method for field analysis of fuel quality. Whereas the original setup was very simple in design, basically integrating a light source, two filters and the smartphone camera as the detector, here, free-form optics were designed and manufactured from **resin 1** to improve the optical read-out (Figure 7a-b, Figure S17, Movie S3). One lens was used to focus the excitation beam from a standard LED at 465 nm, placed at 45° and filtered with a 470 nm bandpass filter. The second lens was used to focus the emission from the strips onto the smartphone camera. The excitation lens is an asymmetric bi-convex cylindrical lens specifically designed to obtain a rectangular beam shape over the position of the test strips. The

emission from the strips is collected from a truncated plano-convex lens with a focal distance of 50 mm. The lens collimates the emission from the strips through a 500 nm long-pass filter to the smartphone camera. Comparison was made with the smartphone case assembly before and after insertion of the free-form optics. In accordance with our previous study,<sup>18</sup> the same protocols for particle and strip preparation were followed, but here a different beacon harpin loop was used for SARS-CoV-2 RNA detection targeting the RdRp-P1 gene (*NC\_004718 SARS Human -related CoV (e.g. Frankfurt-1)*).<sup>55</sup> The molecular beacon oligomer sequence integrated 6-carboxyfluorescein (FAM) as the indicator at one end, 4-((4-(dimethylamino)phenyl)azo)benzoic acid (DABCYL) as the quencher at the other end, plus a modified thymine base ([AmC6dT]) for anchoring of the beacon on the particles: 5'-FAM-TAGAAGCCAGGTGGAACATCATCCGGTGATGCCT[AmC6dT]CTA-DABCYL-3'. An RNA oligomer sequence from the RdRp-P1 gene (5'-GGUCCACCUUGUAGUAGGCCACUACG-3'), complementary to the beacon harpin loop, was used for testing of the sensor. Upon increasing concentration of complementary RNA, a fluorescence enhancement resulting from the separation of the fluorescein reporter dye from the quenching unit could be observed.

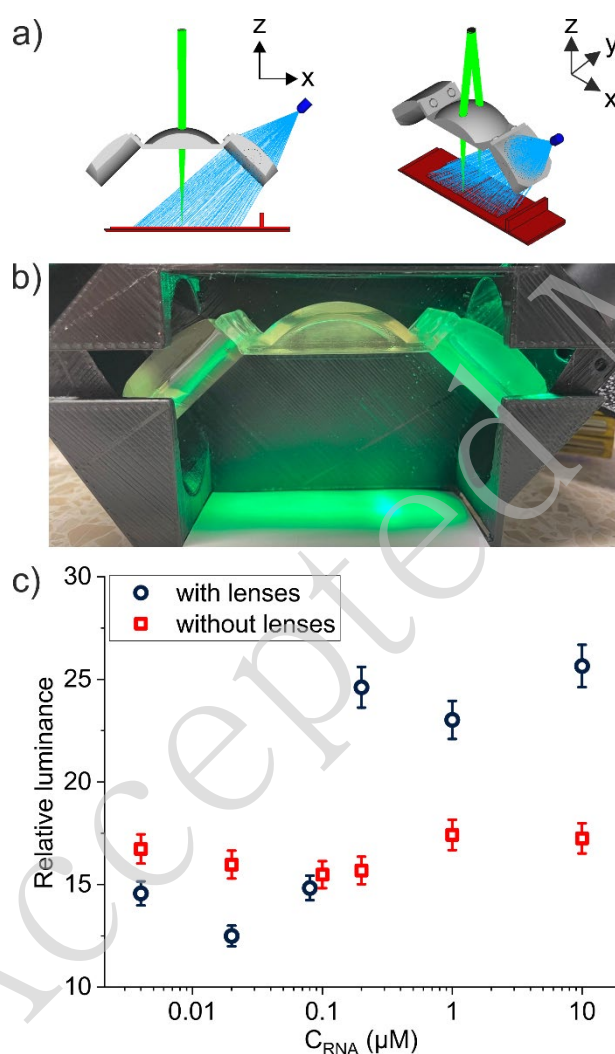


**Figure 7.** a) Ray tracing of the excitation irradiation and emission collection with the dedicated free-form optics. The sketches show the smartphone case inner set up with excitation beam from one LED, the strip's emission, the strip holder and the 3D printed lenses (Filters and 3D printed case are omitted for simplification purposes); b) Photograph of the assembly interior with the free-form optics; c) Assay

response toward SARS-CoV-2 RNA as measured with the optical detection device built with (black circles) or without (red squares) three free-form lenses for read-out enhancement.

As shown in Figure 7c, the results with and without the lenses exhibited a similar background of approx. 40 in relative luminance (Y).<sup>56</sup> The signal experienced a pronounced increase for concentrations above 0.1  $\mu\text{M}$  of complementary DNA when the 3D-printed case integrates free-form lenses. Interestingly, the percentage measurement error remained similar (approx. 4%), indicating that the free-form polymer lenses enabled lower fluorescence signal detection without drastically increasing the noise of the measurement, as a higher digital gain, i.e., a higher ISO value, would do. From the user's perspective, the device has an inflection point or OFF-ON value around 0.1  $\mu\text{M}$ , which corresponds to the response of the beacon-based particles. This value is too high to allow direct detection of viral RNA in saliva (500 copies  $\mu\text{L}^{-1}$ ), but similar to most reported rapid assays,<sup>57, 58</sup> a reasonable number of PCR amplification cycles would allow for screening of infected patients with the developed smartphone based optical device.

## Conclusion

As optical devices for rapid (bio)chemical analysis advance towards increasingly intricate and miniaturized designs, there is an increasing demand for accessible and cost-effective fabrication methods, especially for high-performance optical elements. The present study demonstrates that stereolithography (SLA) 3D printing offers a practical, user-friendly solution for producing high-quality optical components, thereby extending access beyond the confines of specialized laboratories to non-expert users. A simple and robust post-treatment protocol was developed here to enhance the optical properties of manufactured elements, achieving over 85% transmittance, minimal intrinsic fluorescence, low surface roughness, and refractive indexes approaching that of N-BK7 optical glass. This approach facilitates the rapid prototyping of unconventional and free-form optics, thereby supporting the development of advanced optical systems, including opto-sensors. The integration of SLA-printed free-form optics into a smartphone-based detection device of a rapid SARS-CoV-2 assay demonstrates the efficacy of this method in facilitating the development of miniaturized analytical devices by reducing technical barriers. Beyond analysis and sensing, this work paves the way for scalable, cost-effective solutions in microfluidics, imaging, and photonic device fabrication, rendering optical prototyping accessible to researchers across disciplines, including for example chemists and biologists developing sensors but without specialized expertise in optics.

## Acknowledgements

M. A. H. G. thanks BAM for funding (Grant number IE2211)

## Author contributions

M. A. H. G.: Conceptualization, Formal analysis, Investigation, Methodology, Validation, Writing - original draft; K. R.: Conceptualization, Funding acquisition, Resources, Supervision, Writing - review & editing; J. B.: Conceptualization, Funding acquisition, Investigation, Supervision, Writing - review & editing.

## Data availability

The authors declare that the data supporting the findings of this study are available within the paper and its Supplementary Information files. Should any raw data files be needed in another format they are available from the corresponding author upon reasonable request.

## Conflict of interests

The authors declare no conflict of interest.

## References

1. Singh, A. K. et al. Optical biosensors: a decade in review. *Alexandria Engineering Journal* **67**, 673-691 (2023).
2. Chekkaramkodi, D. et al. Review of vat photopolymerization 3D printing of photonic devices. *Additive Manufacturing* **86**, 104189 (2024).
3. Wu, R. M. et al. Design of freeform illumination optics. *Laser & Photonics Reviews* **12**, 1700310 (2018).
4. Kumar, S., Tong, Z. & Jiang, X. Q. Advances in the design and manufacturing of novel freeform optics. *International Journal of Extreme Manufacturing* **4**, 032004 (2022).
5. Freebody, M. Manufacturing methods make freeform optics more accessible. *Photonics Spectra* a69218 (2023). **(Checked all online materials, but the volume and page number information was not found, please contact the author for confirmation)**
6. Reichert, C. et al. Evaluation and comparison of different materials for manufacturing of transparent optical components in additive manufacturing. *Optical Engineering* **60**, 067103 (2021).
7. Beckert, E. et al. Inkjet printing of microlens arrays on large, lithographic structured substrates. Proceedings of SPIE 10930, Advanced Fabrication Technologies for Micro/Nano Optics and Photonics XII. San Francisco, California, United States: SPIE, 2019, 109300C.
8. Balakrishnan, H. K. et al. 3D printing: an alternative microfabrication approach with unprecedented opportunities in design. *Analytical Chemistry* **93**, 350-366 (2021).
9. Bartels, D., Heise, M. & Schmidt, M. Geometrical and optical properties of optical components manufactured by means of stereolithography. *Optics* **5**, 611-621 (2024).
10. Bernal, P. N. et al. The road ahead in materials and technologies for volumetric 3D printing. *Nature Reviews Materials* **10**, 826-841 (2025).
11. Hull, C. W., Apparatus for production of three-dimensional objects by stereolithography, US4575330A, (1984).
12. Jeong, H. Y. et al. 3D and 4D printing for optics and metaphotonics. *Nanophotonics* **9**, 1139-1160 (2020).
13. Ligon, S. C. et al. Polymers for 3D printing and customized additive manufacturing. *Chemical Reviews* **117**, 10212-10290 (2017).
14. Berglund, G. D. & Tkaczyk, T. S. Fabrication of optical components using a consumer-grade lithographic printer. *Optics Express* **27**, 30405-30420 (2019).
15. Wabiński, J. et al. Light transmittance of transparent 3D printing resins. *Applied Research* **4**, e70028 (2025).

16. Mansurova, M. et al. Fluorescent hydrophobic test strips with sterically integrated molecular rotors for the detection of hydrocarbons in water and soil with an embedded optical read-out. *Energy & Fuels* **37**, 10544-10549 (2023).
17. Tillo, A. et al. Microfluidic device for the determination of water chlorination levels combining a fluorescent meso-enamine boron dipyrromethene probe and a microhydrocyclone for gas bubble separation. *Analytical Chemistry* **91**, 12980-12987 (2019).
18. Climent, E. et al. Dip sticks embedding molecular beacon-functionalized core-mesoporous shell particles for the rapid on-site detection of microbiological fuel contamination. *ACS Sensors* **6**, 27-34 (2021).
19. Lakowicz, J. R. Principles of Fluorescence Spectroscopy. (New York: Springer, 2006).
20. Yu, H. R. et al. Front-face fluorescence excitation-emission matrix (FF-EEM) for direct analysis of flocculated suspension without sample preparation in coagulation-ultrafiltration for wastewater reclamation. *Water Research* **187**, 116452 (2020).
21. Hicks, T. Glass Analysis. in Encyclopedia of Forensic Sciences (eds Siegel, J. A., Saukko, P. J. & Houck, M. M.) (Waltham: Academic Press, 2013), 227-232.
22. Salas, A. et al. Chemistry in light-induced 3D printing. *ChemTexts* **9**, 4 (2023).
23. Bagheri, A. & Jin, J. Y. Photopolymerization in 3D printing. *ACS Applied Polymer Materials* **1**, 593-611 (2019).
24. Hosseinzadeh, E. et al. Fabrication of soft transparent patient-specific vascular models with stereolithographic 3D printing and thiol-based photopolymerizable coatings. *Macromolecular Rapid Communications* **45**, 2300611 (2024).
25. Zhu, D. X. et al. 3D printing of customized aspheric lenses for imaging. *Polymers* **13**, 3477 (2021).
26. Tokarczyk, M. et al. Adhesion of varnish coatings as a background for analogue and digital printing technologies. *Applied Sciences* **14**, 304 (2024).
27. Shrotri, A., Preu, S. & Stübbe, O. Achieving transparency and minimizing losses of rough additively manufactured optical components by a dip-coating surface finish. *Coatings* **15**, 210 (2025).
28. Vaidya, N. & Solgaard, O. 3D printed optics with nanometer scale surface roughness. *Microsystems & Nanoengineering* **4**, 18 (2018).
29. Golhin, A. P. et al. Surface roughness of as-printed polymers: a comprehensive review. *The International Journal of Advanced Manufacturing Technology* **127**, 987-1043 (2023).
30. Braun, K., Willenborg, E. & Schleifenbaum, J. H. Laser polishing as a new post process for 3D-printed polymer parts. *Procedia CIRP* **94**, 134-138 (2020).
31. Xie, J. et al. Study on a 5-axis precision and mirror grinding of glass freeform surface without on-machine wheel-profile truing. *International Journal of Machine Tools and Manufacture* **109**, 65-73 (2016).
32. Zhou, J. et al. High-temperature friction characteristics of N-BK7 glass and their correlation with viscoelastic loss modulus. *Ceramics International* **47**, 21414-21424 (2021).
33. Xing, Y. T. et al. Freeform surfaces manufacturing of optical glass by ultrasonic vibration-assisted slow tool servo turning. *Journal of Materials Processing Technology* **324**, 118271 (2024).
34. Hausner, M. Optics Inspections and Tests: A Guide for Optics Inspectors and Designers. (Bellingham, Washington: SPIE Press, 2017).
35. Edmund Optics Inc. Understanding optical specifications. (2025). at <https://www.edmundoptics.com/knowledge-center/application-notes/optics/understanding-optical-specifications>.
36. Zhang, L. C. & Liu, W. D. Precision glass molding: toward an optimal fabrication of optical lenses. *Frontiers of Mechanical Engineering* **12**, 3-17 (2017).
37. Hänig, J. & Weller, B. Experimental investigations and numerical simulations of innovative lightweight glass-plastic-composite panels made of thin glass and PMMA. *Glass Structures & Engineering* **6**, 249-271 (2021).

38. Thorlabs. N-BK7 Bi-convex lenses, uncoated. (2025). at <https://www.thorlabs.com/n-bk7-bi-convex-lenses-uncoated>.
39. Goldman, M. J., Green, W. H. & Kroll, J. H. Chemistry of simple organic peroxy radicals under atmospheric through combustion conditions: role of temperature, pressure, and NO<sub>x</sub> level. *The Journal of Physical Chemistry A* **125**, 10303-10314 (2021).
40. Studer, K. et al. Overcoming oxygen inhibition in UV-curing of acrylate coatings by carbon dioxide inerting, Part I. *Progress in Organic Coatings* **48**, 92-100 (2003).
41. Ligon, S. C. et al. Strategies to reduce oxygen inhibition in photoinduced polymerization. *Chemical Reviews* **114**, 557-589 (2014).
42. Simic, R. et al. Oxygen inhibition of free-radical polymerization is the dominant mechanism behind the "mold effect" on hydrogels. *Soft Matter* **17**, 6394-6403 (2021).
43. Segurola, J. et al. Photoyellowing and discolouration of UV cured acrylated clear coatings systems: influence of photoinitiator type. *Polymer Degradation and Stability* **64**, 39-48 (1999).
44. Arsu, N., Stephen Davidson, R. & Holman, R. Factors affecting the photoyellowing which occurs during the photoinitiated polymerization of acrylates. *Journal of Photochemistry and Photobiology A: Chemistry* **87**, 169-175 (1995).
45. Nan, X. Y. et al. Different photoinitiating ability and photobleaching efficiency of erythrosine B derivatives in radical/cationic photopolymerization. *Fibers and Polymers* **18**, 1644-1651 (2017).
46. Dumur, F. Recent advances on photobleachable visible light photoinitiators of polymerization. *European Polymer Journal* **186**, 111874 (2023).
47. Asmussen, S. et al. Photoinitiation rate profiles during polymerization of a dimethacrylate-based resin photoinitiated with camphorquinone/amine. Influence of initiator photobleaching rate. *European Polymer Journal* **45**, 515-522 (2009).
48. Sun, G. Q., Wu, X. Y. & Liu, R. A comprehensive investigation of acrylates photopolymerization shrinkage stress from micro and macro perspectives by real time MIR-photo-rheology. *Progress in Organic Coatings* **155**, 106229 (2021).
49. Marx, P. & Wiesbrock, F. Expanding monomers as anti-shrinkage additives. *Polymers* **13**, 806 (2021).
50. Green, W. A. *Industrial Photoinitiators: A Technical Guide*. (Boca Raton: CRC Press, 2010).
51. Wiesner, T. & Haas, M. Do germanium-based photoinitiators have the potential to replace the well-established acylphosphine oxides? *Dalton Transactions* **50**, 12392-12398 (2021).
52. Müller, S. M. et al. Recent advances in type i photoinitiators for visible light induced photopolymerization. *ChemPhotoChem* **6**, e202200091 (2022).
53. Meyzonnette, J. L., Mangin, J. & Cathelinaud, M. Refractive index of optical materials. in *Springer Handbook of Glass* (eds Musgraves, J. D., Hu, J. J. & Calvez, L.) (Cham: Springer, 2019), 997-1045.
54. Rurack, K. & Spieles, M. Fluorescence quantum yields of a series of red and near-infrared dyes emitting at 600-1000 nm. *Analytical Chemistry* **83**, 1232-1242 (2011).
55. Corman, V. M. et al. Detection of 2019 novel coronavirus (2019-nCoV) by real-time RT-PCR. *Eurosurveillance* **25**, 2000045 (2020).
56. Gotor, R. et al. Detection of adulterated diesel using fluorescent test strips and smartphone readout. *Energy & Fuels* **31**, 11594-11600 (2017).
57. Alenquer, M. et al. Saliva molecular testing bypassing RNA extraction is suitable for monitoring and diagnosing SARS-CoV-2 infection in children. *PLoS One* **17**, e0268388 (2022).
58. Allicock, O. M. et al. Pooled RNA-extraction-free testing of saliva for the detection of SARS-CoV-2. *Scientific Reports* **13**, 7426 (2023).